2007

Room-Temperature Electron Spin Dynamics in Free-Standing ZnO Quantum Dots

W. K. Liu
K. M. Whitaker
A. L Smith
Kevin R. Kittilstved, *University of Massachusetts - Amherst*
B. H. Robinson, et al.

Room-Temperature Electron Spin Dynamics in Free-Standing ZnO Quantum Dots

William K. Liu, Kelly M. Whitaker, Alyssa L. Smith, Kevin R. Kittilstved, Bruce H. Robinson, and Daniel R. Gamelin*

Department of Chemistry and Center for Nanotechnology, University of Washington, Seattle, Washington 98195, USA

(Received 30 January 2007; published 2 May 2007)

Conduction band electrons in colloidal ZnO quantum dots have been prepared photochemically and examined by electron paramagnetic resonance spectroscopy. Nanocrystals of 4.6 nm diameter containing single *S*-shell conduction band electrons have $g^* = 1.962$ and a room-temperature ensemble spin-dephasing time of $T_2^* = 25$ ns, as determined from linewidth analysis. Increasing the electron population leads to increased g^* and decreased T_2^*, both associated with formation of *P*-shell configurations. A clear relationship between T_2^* and hyperfine coupling with ^{67}Zn($I = 5/2$) is observed.

DOI: 10.1103/PhysRevLett.98.186804 PACS numbers: 73.21.La, 73.22.−f, 76.30.−v, 85.75.−d

Electron spins in semiconductor quantum dots (QDs) are promising candidates for information processing using quantum particles (quantum computation) [1]. An attraction of this motif is the slower spin-dephasing expected upon electron confinement. In QDs, dephasing mechanisms involving spin-orbit coupling are believed to be suppressed, making electron-nuclear hyperfine coupling the dominant source of spin relaxation [2,3]. In this Letter, we describe the use of electron paramagnetic resonance (EPR) spectroscopy to probe electron spin dynamics in colloidal QDs of ZnO, a prototype wide-gap semiconductor. With its well-defined doping and defect chemistries, suitability for transparent high-power high-temperature applications, and ability to lase at ultraviolet (UV) wavelengths, ZnO is attractive for many potential applications [4]. Recently, relatively long room-temperature spin-dephasing times ($T_2^* \leq 0.19$ ns) have been measured for bulk and epitaxial *n*-type ZnO using time-resolved Faraday rotation (TRFR) spectroscopy [5], but to date no studies of spin dynamics in ZnO nanostructures have been reported. Here, T_2^* has been measured at room-temperature for freestanding ZnO QDs containing between 1 and 6 additional conduction band electrons. Values up to 25 ns, or ~125 times longer than in bulk or thin-film ZnO, are observed. The hypothesis that electron-nuclear hyperfine interactions dominate spin-dephasing dynamics is confirmed directly by variation of the ^{67}Zn($I = 5/2$) content.

Freestanding ZnO QDs capped with trioctylphosphine oxide (TOPO) and suspended in toluene were prepared, charged, and characterized as described previously [6,7]. Conduction band electrons (e^-_{CB}) were generated by UV irradiation in the presence of ethanol, a hole scavenger [8], under rigorously anaerobic conditions [7].

Figure 1(a) shows a photograph of as-prepared (ZnO) and charged (e^-_{CB}: ZnO) colloidal ZnO QDs. Figure 1(b) shows 298 K electronic absorption spectra collected before and after UV irradiation. With irradiation, the first excitonic peak in the UV was bleached, and a broad NIR absorption band of comparable oscillator strength appeared. The bluish hue visible by eye in the charged nanocrystals is due to tailing of this NIR band into the visible region. These spectral changes, prominent in the absorption difference spectrum (charged—as-prepared, Fig. 1(c)), agree well with those reported previously [7,9,10]. The UV bleaching has been attributed to electron filling of the conduction band, and the new NIR intensity to dipole-allowed intra-conduction-band excitation [9,10]. The multiple sharp absorption peaks in the NIR are solvent vibrational overtones. When kept anaerobic, the charged ZnO nanocrystals are kinetically very stable ($k_{decay} <$ 0.01/week at 298 K), but they return rapidly and com-

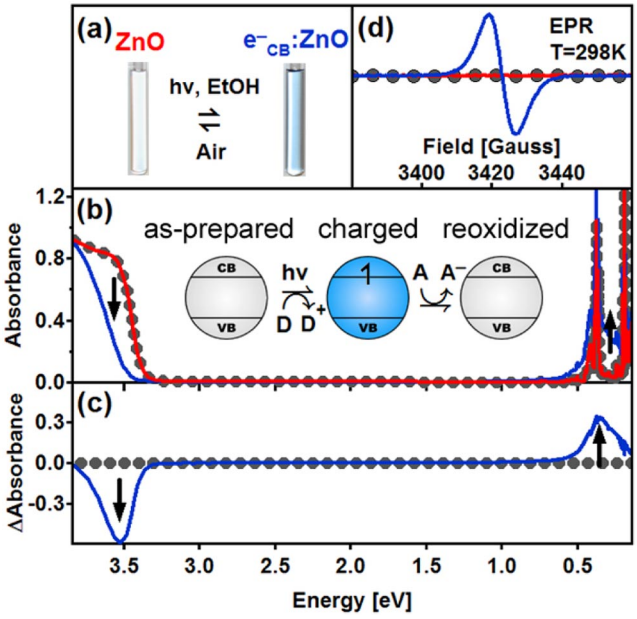

FIG. 1 (color online). (a) Photographs of as-prepared and charged colloidal ZnO QDs. (b) The 298 K absorption spectra of as-prepared (solid line), charged (solid line, arrows), and reoxidized (filled circles) colloidal ZnO QDs. (c) Difference absorption spectra showing UV bleaching and IR absorption with charging (solid line, arrows) and reversal with reoxidation (filled circles). (d) The 298 K EPR spectra of as-prepared (solid line, no signal), charged (solid line), and reoxidized (filled circles) colloidal ZnO QDs.

pletely to their initial forms upon exposure to air (gray dots in Fig. 1(b) and 1(c)]. This facile reversibility demonstrates that no photodegradation occurs under these charging conditions.

Figure 1(d) shows the 298 K X-band (9.5 GHz) EPR spectra of colloidal ZnO nanocrystals before and after charging. The as-prepared ZnO nanocrystals showed no EPR signal. After UV irradiation, an intense new EPR signal at $g^* \approx 1.96$ was detected, similar to those reported in nano- and microcrystalline aggregates of ZnO [11–13]. Since n-type grain-boundary defects are abundant in ZnO aggregates and may severely complicate analysis of their EPR spectra, TOPO-capped ZnO nanocrystals [6,7] were used here to ensure that the physical properties observed are those of the freestanding QDs. The deviation from $g_e = 2.0023$ indicates that the new EPR signal in Fig. 1(d) does not originate from deeply trapped electrons. From $K \cdot P$ treatment of the ZnO band structure (Eq. (1), [13,14]), the reduction of g^* derives from the combination of interband mixing (P) and spin-orbit coupling (Δ), both of which are relatively small in ZnO. From Eq. (1), g^* also depends on QD diameter since the energy gap (E_g) is size dependent [13,14]. As with the NIR absorption, the $g^* = 1.96$ signal disappeared upon exposure of the charged QDs to air (Fig. 1(d)). Collectively, the data in Fig. 1 confirm that the added electrons reside in the ZnO QD conduction band. One electron in a $d = 4.6$ nm QD corresponds to a carrier density of 2×10^{19} cm^{-3}.

$$g^* = g_e - \frac{2}{3}\left(\frac{P^2\Delta}{E_g(E_g + \Delta)}\right) \tag{1}$$

Both the NIR absorption and $g^* = 1.96$ EPR intensities increase with increasing UV irradiation times. Interestingly, plots of EPR vs NIR intensities are not linear. To understand this observation, the average number of electrons per ZnO nanocrystal ($\langle n \rangle$) was determined for several samples by titration with recrystallized methyl viologen dichloride [15]. Whereas the rate of change of the integrated NIR intensity increases slightly with increasing $\langle n \rangle$, the data in Fig. 2(a) show a pronounced curvature in the EPR intensity with increasing $\langle n \rangle$. Tight-binding calculations [16] describe the lowest conduction energy levels of ZnO quantum dots as having S, P, and D symmetries with orbital degeneracies of 2, 6, and 10, respectively. To analyze the data in Fig. 2(a), it was assumed that electron filling of these levels in each QD follows the Aufbau principle (as observed with electrochemical charging [16]) and Hund's rules, and that Poissonian statistics govern electron distributions over the ensemble of QDs. To test these assumptions, spin-weighted Poissonian population distributions were calculated using Eq. (2). Here, n is the number of electrons in a given QD and α represents the number of possible EPR transitions allowed ($\Delta M_s = \pm 1$) in the resulting multielectron configuration. Equation (2) thus allows estimation of the EPR intensity as a function of average electron occupancy $\langle n \rangle$ within the Poissonian filling model.

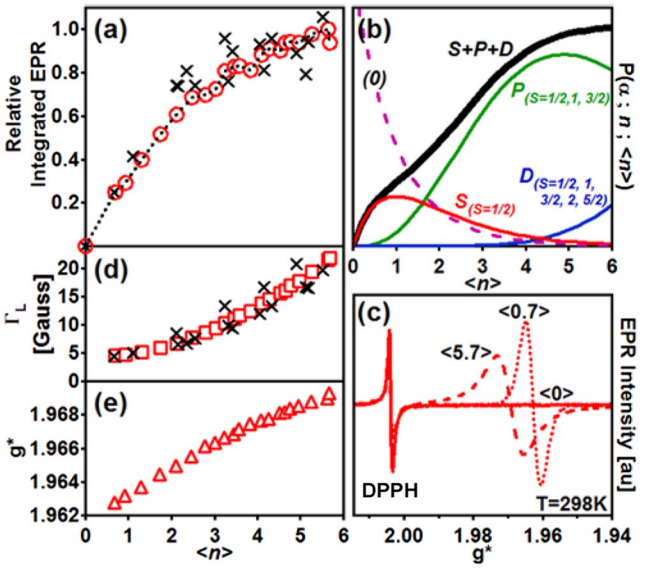

FIG. 2 (color online). EPR spectra of colloidal ZnO QDs ($d = 4.6 \pm 0.4$ nm, 298 K) as a function of $\langle n \rangle$. (a) Relative double integration of the first-derivative EPR intensities. Data for which $\langle n \rangle$ was determined by chemical titration are marked $\times$. (b) Spin-weighted Poissonian probabilities for S, P, and D filling in an ensemble of ZnO QDs. (c) EPR spectra of as-prepared (solid line), low $\langle n \rangle$ (filled circles), and high $\langle n \rangle$ (dashed line) ZnO QDs (DPPH = internal standard, $g = 2.0037 \pm 0.0002$). (d) Lorentzian line widths. (e) e^-_{CB} g^* values.

$$P(\alpha; n; \langle n \rangle) = \alpha \frac{\langle n \rangle^n e^{-\langle n \rangle}}{n!} \tag{2}$$

The sum of spin-weighted populations calculated for all of the EPR active configurations [$S(S = 1/2)$, $P(S = 1/2, 1, 3/2)$, and $D(S = 1/2, 1, 3/2, 2, 5/2)$] is plotted vs $\langle n \rangle$ in Fig. 2(b). The calculated curve reproduces the experimental data (Fig. 2(a)) remarkably well. The minor differences in curvature are reasonable given the simplicity of the model, since non-Poissonian populations due to the finite particle size distribution may be reasonably anticipated. Notably, curves calculated excluding either $S = 1$ (non-Kramers) or all $S > 1/2$ configurations fail to reproduce the experimental curvature of Fig. 2(a) adequately, suggesting that zero-field splittings of the $S > 1/2$ configurations are small relative to the X-band photon energy. The curvature in Fig. 2(a) thus ultimately reflects differences between *unpaired* and *total* ($\langle n \rangle$) electron populations in charged QDs with level filling governed predominantly by Poissonian statistics. These conclusions are supported by use of the same statistical model to analyze the change in NIR intensity with $\langle n \rangle$, which yields ~ 0.25 for the relative S-P:P-D oscillator strengths, in good agreement with the published ratio (~ 0.33) [17].

The e^-_{CB} EPR signal is substantially broader than that of the internal reference DPPH (diphenylpicrylhydrazyl radical) at all values of $\langle n \rangle$ (Fig. 2(c)). Although the EPR line shapes are nearly Lorentzian, analysis reveals some inhomogeneous broadening, as might be expected from the finite QD size distribution and the size dependence of g^* (Eq. (1)). For analysis of the linewidths, the homogeneous (Γ_L, Lorentzian fwhh) and inhomogeneous ($\Gamma_{\Delta g^*}$, Gaussian standard deviation) contributions to the lineshape in each EPR spectrum were therefore deconvolved. The resulting homogeneous linewidths are plotted vs $\langle n \rangle$ in Fig. 2(d). Whereas Γ_L increases with increasing $\langle n \rangle$, $\Gamma_{\Delta g^*}$ remains small and nearly constant ($1.5 < \Gamma_{\Delta g^*} < 3.3$ G) over the entire range of $\langle n \rangle$ [18]. This broadening and the concomitant g^* shift (Fig. 2(e)) with increasing $\langle n \rangle$ are discussed in more detail below.

The e^-_{CB}:ZnO EPR linewidths are of fundamental importance since they directly reflect electron spin dynamics. The longitudinal relaxation time (T_1) for the charged ZnO QDs was investigated by pulse saturation recovery (Fig. 3(a)) [19] and saturation rollover EPR measurements (not shown). Both experiments show T_1 to be on the microsecond time scale at 298 K. To a good approximation, Γ_L is then related to the ensemble spin-dephasing time T_2^* according to Eq. (3). From $\Gamma_L = 4.54$ G measured for $\langle n \rangle = 0.7$ at 298 K, $T_2^* = 25$ ns is determined. This T_2^* is ~125 times greater than those measured for bulk and epitaxial n-type ZnO by TRFR spectroscopy at 290 K ($T_2^* \leq 0.19$ ns) [5].

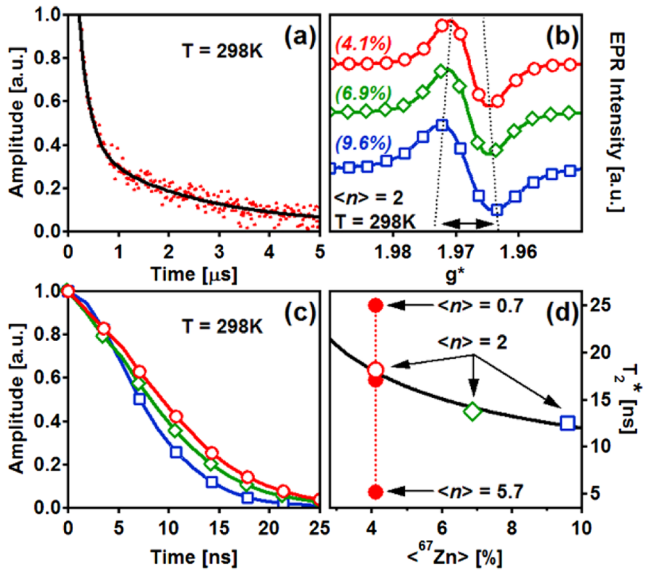

FIG. 3 (color online). (a) Pulse saturation recovery EPR data for natural abundance ZnO QDs. The solid line shows a biexponential best fit with $\tau_a = 0.24$ and $\tau_b = 2.7$ μs. (b) e^-_{CB}: ZnO QD EPR signal as a function of $\langle {}^{67}\mathrm{Zn} \rangle$ for $d = 4.0 \pm 0.4$ nm QDs with $\langle n \rangle = 2$. (○) 4.1% (natural abundance), (◇) 6.8%, and (□) 9.6% ^{67}Zn. The dotted lines are guides to the eye. (c) Fourier transforms of EPR absorption spectra from (b). (d) Plot of Γ_L vs $\langle {}^{67}\mathrm{Zn} \rangle$ for the data from (b). The solid line plots $T_2^* = (c\sqrt{\langle {}^{67}\mathrm{Zn} \rangle})^{-1}$.

$$T_2^* = \frac{2\hbar}{g_e \mu_B \Gamma_L} \tag{3}$$

In GaAs, InAs, and CdSe QDs, spin dephasing has been associated with the electron-nuclear hyperfine interaction [2,3], which is large in these lattices because many of their ions have nuclear spin. Following Ref. [2], T_2^* in this scenario depends on the strength and number of hyperfine interactions in the QD as described by Eq. (4), where N_L is the total number of ions in the QD, n is the number of ions in the unit cell, I^j is the nuclear spin on the j-th ion, A^j is the hyperfine coupling constant at the j-th ion, and the sum is over all ions in the unit cell.

$$T_2^* = \hbar \sqrt{\frac{3N_L}{2n \sum_j I^j (I^j + 1)(A^j)^2}} \tag{4}$$

In contrast with GaAs, InAs, or CdSe, the vast majority of cations and anions in ZnO have $I = 0$. Only ^{67}Zn ($I = 5/2$, 4.1% natural abundance) may contribute significantly to spin dephasing via the hyperfine interaction. To test the hypothesis that the linewidth shown in Fig. 2 depends on electron-nuclear hyperfine coupling, a series of 4.0 ± 0.4 nm diameter nanocrystal samples having different average ^{67}Zn contents ($\langle {}^{67}\mathrm{Zn} \rangle$) have been synthesized by starting from ^{67}Zn-enriched $Zn(OAc)_2$ precursors. Each sample was prepared and charged to $\langle n \rangle = 2$ under identical conditions. The resulting EPR spectra are plotted in Fig. 3(b). Clearly, increasing $\langle {}^{67}\mathrm{Zn} \rangle$ from 4.1 to 9.6% increases the linewidth substantially. This increase corresponds to a decreased spin-dephasing time, as evident from plots of the Fourier transformed EPR absorption spectra for the same three samples (Fig. 3(c)). The data in Fig. 3(c) include both Γ_L and $\Gamma_{\Delta g^*}$ linewidth contributions. To examine the influence of $\langle {}^{67}\mathrm{Zn} \rangle$ more quantitatively, Γ_L and $\Gamma_{\Delta g^*}$ were deconvolved and T_2^* analyzed according to Eq. (3).

Figure 3(d) plots T_2^* vs $\langle {}^{67}\mathrm{Zn} \rangle$ for the three $\langle n \rangle = 2$ QD samples from Fig. 3(b). T_2^* decreases from 18 to 13 ns upon increasing $\langle {}^{67}\mathrm{Zn} \rangle$ from 4.1 to 9.6%. The solid line shows the best fit of the function $T_2^* = (c\sqrt{\langle {}^{67}\mathrm{Zn} \rangle})^{-1}$ (from Eq. (4)) to the data, where c is a constant. The excellent fit demonstrates that hyperfine coupling with ^{67}Zn is responsible for the majority of the room-temperature e^-_{CB} EPR linewidth (and hence also T_2^*) in these e^-_{CB}: ZnO QDs. Extrapolation of the fit from Fig. 3(d) allows estimation of $T_2^* \approx 100$ ns for $\langle n \rangle = 2$ and $\langle {}^{67}\mathrm{Zn} \rangle = 0$. These results indicate that long room-temperature electron spin-dephasing times can be achieved in QDs by chemical modification to eliminate ions with $I \neq 0$.

In addition to hyperfine coupling, overcharging is very effective in reducing T_2^*. The vertical dashed line in

Fig. 3(d) plots T_2^* for the same QD sample at three charging levels, $\langle n \rangle = 0.7$, 2.0, and 5.7 (from Fig. 2(d)), showing T_2^* reduction from 25 to 17 and 5 ns, respectively. Although quantitative analysis is complicated by the ensemble nature of the experiment, it is evident from comparison of Figs. 2(b) and 2(d) that T_2^* decreases as the unpaired e_{CB}^- population shifts from predominantly S to predominantly P configurations. Since line broadening occurs only above $\langle n \rangle \approx 1.5$, where multielectron P configurations begin to appear, it is concluded that spin-spin relaxation mechanisms are predominantly responsible for the reduction in T_2^* with increasing $\langle n \rangle$. Finally, the data in Fig. 2(e) reveal that g^* is greater for P electrons than for an unpaired S electron. The Poissonian analysis allows resolution of individual g^* values from the data in Fig. 2(e), yielding $g^*(S^1) = 1.962$ and $g^*(S^2P^1) = 1.971$. This increase is also evident from the comparison of $g^* = 1.968$ at $\langle n \rangle = 4.4$, where ~93% of the EPR intensity derives from P configurations, with $g^* = 1.963$ at $\langle n \rangle = 0.7$, where ~86% of the EPR intensity derives from the S^1 configuration. The increasing g^* may reflect contributions from orbital angular momentum in the P configurations. Indeed, calculations on spherical ZnO nanocrystals within the multiband effective mass approximation have predicted substantial orbital effective Landé g factors for P electrons ($l = 1$) [14]. Future experiments will seek to describe these highly charged QDs in greater detail.

Overall, the longest room-temperature spin-dephasing time observed experimentally is $T_2^* = 25$ ns for a single electron ($\langle n \rangle = 0.7$) in the $d = 4.6$ nm ZnO QDs with natural abundance $\langle {}^{67}\mathrm{Zn} \rangle = 4.1\%$ (Fig. 3(d)). The isotropic hyperfine coupling for an electron localized on ${}^{67}\mathrm{Zn}$ has been reported as $A({}^{67}\mathrm{Zn}) = 5.17$ μeV [20]. With $N_L \approx 4300$, Eq. (4) yields $T_2^* = 6.0$ ns. Although the calculated T_2^* is a factor of 4 smaller than the experimental value, the two are in reasonable agreement given that (i) covalency will decrease $A({}^{67}\mathrm{Zn})$ and (ii) crystal shape anisotropy may cause the real e_{CB}^- wave function to deviate from the idealized wave function assumed in derivation of Eq. (4) [2]. The accurate functional dependence of T_2^* on $\langle {}^{67}\mathrm{Zn} \rangle$ predicted by Eq. (4) in Fig. 3(d) confirms the role of hyperfine coupling in determining T_2^* in these charged QDs.

In summary, electron spin dynamics in ZnO QDs have been probed by EPR spectroscopy. T_2^* values up to 25 ns at 298 K have been observed, and a clear relationship between T_2^* and e_{CB}^--${}^{67}\mathrm{Zn}$ hyperfine coupling has been demonstrated. These results point to chemical control over $\langle {}^{67}\mathrm{Zn} \rangle$ as a promising avenue for increasing T_2^* in ZnO QDs. More generally, chemical preparation of freestanding charged QDs has been shown to offer rich opportunities for exploration of spin dynamics in semiconductor nanostructures related to quantum computation and spintronics.

This work was funded by the NSF (No. DMR-0239325 to D. R. G. and No. DGE-0504573 (IGERT) to K. M. W.), the Research Corporation, the Dreyfus Foundation, and the Sloan Foundation. Instrumentation support from the Center for Ecogenetics and Environmental Health UW Center Grant No. P30 ES07033 from the National Institutes of Environmental Health Sciences, NIH, is gratefully acknowledged.

*Electronic address: Gamelin@chem.washington.edu

[1] V. Cerletti, W. A. Coish, O. Gywat, and D. Loss, Nanotechnology **16**, R27 (2005), and references therein.
[2] I. A. Merkulov, A. L. Efros, and M. Rosen, Phys. Rev. B **65**, 205309 (2002).
[3] P.-F. Braun, X. Marie, L. Lombez, B. Urbaszek, T. Amand, P. Renucci, V. K. Kalevich, K. V. Kavokin, O. Krebs, P. Voisin, and Y. Matsumoto, Phys. Rev. Lett. **94**, 116601 (2005).
[4] D. C. Look and B. Claflin, Phys. Status Solidi (b) **241**, 624 (2004).
[5] S. Ghosh, V. Sih, W. H. Lau, D. D. Awschalom, S.-Y. Bae, S. Wang, S. Vaidya, and G. Chapline, Appl. Phys. Lett. **86**, 232507 (2005).
[6] D. A. Schwartz, N. S. Norberg, Q. P. Nguyen, J. M. Parker, and D. R. Gamelin, J. Am. Chem. Soc. **125**, 13205 (2003).
[7] W. K. Liu, K. M. Whitaker, K. R. Kittilstved, and D. R. Gamelin, J. Am. Chem. Soc. **128**, 3910 (2006).
[8] M. Haase, H. Weller, and A. Henglein, J. Phys. Chem. **92**, 482 (1988).
[9] M. Shim and P. Guyot-Sionnest, J. Am. Chem. Soc. **123**, 11651 (2001).
[10] A. Germeau, A. L. Roest, D. Vanmaekelbergh, G. Allan, C. Delerue, and E. A. Meulenkamp, Phys. Rev. Lett. **90**, 097401 (2003).
[11] J. Cunningham and S. Corkery, J. Phys. Chem. **79**, 933 (1975).
[12] S. B. Orlinskii, J. Schmidt, P. G. Baranov, D. M. Hofmann, C. d. M. Donegá, and A. Meijerink, Phys. Rev. Lett. **92**, 047603 (2004).
[13] H. Zhou, A. Hofstaetter, D. M. Hofmann, and B. K. Meyer, Microelectron. Eng. **66**, 59 (2003).
[14] A. V. Rodina, A. L. Efros, M. Rosen, and B. K. Meyer, Mater. Sci. Eng., C **19**, 435 (2002).
[15] P. Hoyer and H. Weller, Chem. Phys. Lett. **221**, 379 (1994).
[16] A. L. Roest, A. Germeau, J. J. Kelly, D. Vanmaekelbergh, G. Allan, and E. A. Meulenkamp, Chem. Phys. Chem. **4**, 959 (2003).
[17] A. Germeau, A. L. Roest, D. Vanmaekelbergh, G. Allan, C. Delerue, and E. A. Meulenkamp, Phys. Rev. Lett. **90**, 097401 (2003).
[18] Control experiments show that these EPR spectra are independent of QD concentration in our experimental range, ruling out artifacts from interparticle interactions.
[19] R. D. Nielsen, S. Canaan, J. A. Gladden, M. H. Gelb, C. Mailer, and B. H. Robinson, J. Magn. Reson. **169**, 129 (2004).
[20] J. E. Wertz and J. R. Bolton, *Electron Spin Resonance* (McGraw-Hill, N.Y., 1972).